Wormhole Shadows in Rotating Dust

Takayuki Ohgami* and Nobuyuki Sakai†
Graduate School of Science and Engineering, Yamaguchi University, Yamaguchi 753-8512, Japan

As an extension of our previous work, which investigated the shadows of the Ellis wormhole surrounded by nonrotating dust, in this paper we study wormhole shadows in rotating dust flow. First, we derive steady-state solutions of slowly rotating dust surrounding the wormhole by solving relativistic Euler equations. Solving null geodesic equations and radiation transfer equations, we investigate the images of the wormhole surrounded by dust for the above steady-state solutions. Because the Ellis wormhole spacetime possesses unstable circular orbits of photons, a bright ring appears in the image, just as in Schwarzschild spacetime. The bright ring looks distorted due to rotation. Aside from the bright ring, there appear weakly luminous complex patterns by the emission from the other side of the throat. These structure could be detected by high-resolution very-long-baseline-interferometry observations in the near future.

PACS numbers: 04.40.-b, 97.60.Lf

arXiv:1704.07093v1 [gr-qc] 24 Apr 2017

I. INTRODUCTION

A wormhole is a tunnel-like structure which connects two distant or disconnected regions. A spacetime with nontrivial topology such as a wormhole is approved by general relativity and other extended gravitational theories. The Einstein-Rosen bridge, which is considered as a first wormhole solution of Einstein equations, was discovered by Einstein and Rosen. Because this wormhole is not traversable, it was regarded as nothing but a mathematical product [1]. Several decades later, Ellis [2] obtained a new wormhole solution: a spherically symmetrical solution of Einstein equations with a ghost massless scalar field. Morris and Thorne [3] showed that the Ellis wormhole is one of the traversable wormholes. These wormholes have neither singularity nor horizon; their tidal force is so weak that people can withstand. If such wormholes exist, they could become a fascinating tool for voyaging to far galaxies or engaging in time travel by passing through that.

The stability of traversable wormholes such as Ellis wormholes have been studied by several researchers. Shinkai and Hayward [4] showed the instability of Ellis wormhole by numerical simulations. González *et al.* [5] considered the more general wormholes with the ghost scaler field are also unstable. These researches indicated that Ellis wormholes and other traversable wormhole with a ghost scaler field are practically nonexistent. However, Das and Kar [6] pointed out that another matter could contribute to supporting the Ellis geometry. Furthermore, under the modified gravitational theories, matter such as a ghost scaler field, which makes wormhole spacetimes unstable, may not be required. Therefore, traversable wormholes are still a viable subject not only in theoretical physics, but also in observational astrophysics.

A possible method for probing wormholes is based on gravitational lensing effects. Basic properties of their gravitational lensing effects were investigated theoretically in Ref.[7]. Since Cramer *et al.* [8] pointed out anomalous features of the light curve of a distant star lensed by a wormhole, observational research to find wormholes by using the microlensing effect has proceeded [9]. In addition to the light curve, the lensed images [10] and the lensed spectra [11] of Ellis wormholes have also been discussed as observable quantities.

In a case of probe for blackholes by electromagnetic observations, another method is the usage of shadows, which are the images of optical or radio sources around a blackhole. Blackhole shadows were originally discussed by Bardeen [12] and have recently attracted much attention [13]. This phenomenon has been researched not only theoretically but also observationally by very-long-baseline-interferometry (VLBI) for probing blackholes [14]. Therefore, we expect shadows as many properties of probing Ellis wormholes by use of VLBI observations. Nedkova, Tinchev and Yazadjiev researched shadows caused by a rotating wormhole [15]. They calculated the outline of wormhole in the widely distributed light source.

It is known that photon orbit on the Ellis wormhole spacetime has unstable circular orbits. The existence of this orbit is important for optically observations and the brightly ring appears in the optical image of the wormhole surrounded by the optically thin light source: we discuss in Sec. III. We have considered a case that dust has radial momentum only, and computed the optical image of the wormhole surrounded by optically thin dust [17]. In this paper, we assume that dust has not only radial momentum but also angular momentum. This assumption is more natural state than the former case.

This paper is organized as follows. In Sec. II, we introduce the Ellis wormhole and discuss its spacetime structure. In Sec. III, we derive null geodesic equations and discuss photon trajectories around the Ellis wormhole. In Sec. IV, to set up dust models used in our shadow analysis, we derive steady-state solutions of dust surrounding

*Electronic address: v501wa@yamaguchi-u.ac.jp
†Electronic address: nsakai@yamaguchi-u.ac.jp

the wormhole by solving relativistic Euler equations. In Sec. V, we investigate—by solving the radiative transfer equation along the null geodesic—the images of wormhole surrounded by dust for the models obtained in Sec. IV. Section VI is devoted to concluding remarks.

II. ELLIS WORMHOLE

The Ellis wormhole is the spacetime structure discussed by the line element

$$ds^2 = -dt^2 + dr^2 + (r^2 + a^2)(d\theta^2 + \sin^2\theta\, d\varphi^2), \quad (2.1)$$

where a is the throat radius of wormhole and we adopt the unit system of $c = 1$. People can pass through this wormhole alive because it has neither horizon nor singularity. We draw the embedded diagram of the two-dimensional wormhole surface in the three-dimensional Euclidean space to understand visualy this spacetime structure. Introducing a new radial coordinate,

$$r^* \equiv \sqrt{r^2 + a^2}, \quad (2.2)$$

we express the two-dimensional wormhole surface of t, $\theta = \text{const.}$ by the line element

$$ds_{\rm WH}{}^2 = \frac{1}{1 - a^2/r^{*2}} dr^{*2} + r^{*2} d\varphi^2. \quad (2.3)$$

And then, the line element of three-dimensional Euclidean space described by cylindrical coordinates is given by

$$ds_{\rm ES}{}^2 = dz^2 + dr^{*2} + r^{*2} d\varphi^2. \quad (2.4)$$

Assuming these line elements are equal $ds_{\rm WH} = ds_{\rm ES}$, we obtain the relation

$$z = \pm a \cdot \text{arccosh}\frac{r^*}{a}. \quad (2.5)$$

Figure 1 is a graph of Eq.(2.5) with the φ direction, which indicates the visual image of the spacetime structure of the Ellis wormhole. Two various spaces are connected by the Ellis wormhole like a tunnel. If the wormhole exists in our three-dimensional space, we observe the throat as ball shaped like structure.

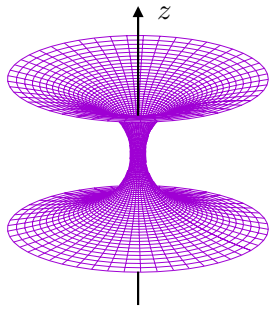

FIG. 1: Diagram of two-dimensional Ellis wormhole curve surface embedded in three-dimensional Euclidean space: plot of z vs. r^* in Eq.(2.5) with the φ direction. It shows that two various spaces are connected by the Ellis wormhole like a tunnel.

III. PHOTON TRAJECTORIES

In preparation to investigate shadow phenomena, we review basic properties of the photon trajectories, which was discussed in Ref.[16, 17].

A. Null geodesic equations and effective potential

Null geodesic equations are generally described as

$$\frac{dk^\mu}{d\lambda} + \Gamma^\mu_{\nu\sigma} k^\nu k^\sigma = 0, \quad \text{with} \quad k_\mu k^\mu = 0, \quad (3.1)$$

where λ, $k^\mu \equiv dx^\mu/d\lambda$ and $\Gamma^\mu_{\nu\sigma}$ are the affine parameter, the null vector and the Christoffel symbol, respectively. The null geodesics in the $\theta = \pi/2$ plane are given by

$$\frac{dk^t}{d\lambda} = 0, \quad \frac{d}{d\lambda}\left\{(r^2 + a^2)k^\varphi\right\} = 0, \quad (3.2)$$

$$\frac{dk^r}{d\lambda} - rk^{\varphi 2} = 0, \quad (3.3)$$

$$-k^{t2} + k^{r2} + (r^2 + a^2)k^{\varphi 2} = 0. \quad (3.4)$$

We need not solve Eq.(3.3) because it can be derived from Eq.(3.2) and (3.4). Integrating Eq.(3.2) with respect to the affine parameter, we obtain conserved quantities E and L as

$$E = k^t, \quad L = (r^2 + a^2)k^\varphi. \quad (3.5)$$

Plugging these quantities into Eq.(3.4), we derive the equation corresponding to the energy conservation as

$$k^{r2} + V_{\rm eff}(r) = E^2, \quad V_{\rm eff}(r) \equiv \frac{L^2}{r^2 + a^2}. \quad (3.6)$$

Figure 2 shows the graph of the effective potential $V_{\rm eff}$. This graph is useful for discussing photon trajectories.

B. Photon trajectories

The trajectories are classified into three types A, B, and C, as shown in Fig.2. Type A trajectories do not hit the wall of the potential and go into the region of $r < 0$ from that of $r > 0$; this means that the photons pass through the wormhole into the other side. Type B trajectories approach the local maximum of the potential; this means that the the photons rotate around the throat infinite times in approaching the throat. Considering time reversal, we can interpret that any photon which rotates around $r = 0$ is unstable and eventually goes into $r \to \infty$ or $r \to -\infty$. Type C trajectories bounce from the wall of potential and goes to infinity; in this case light rays are refracted by gravity.

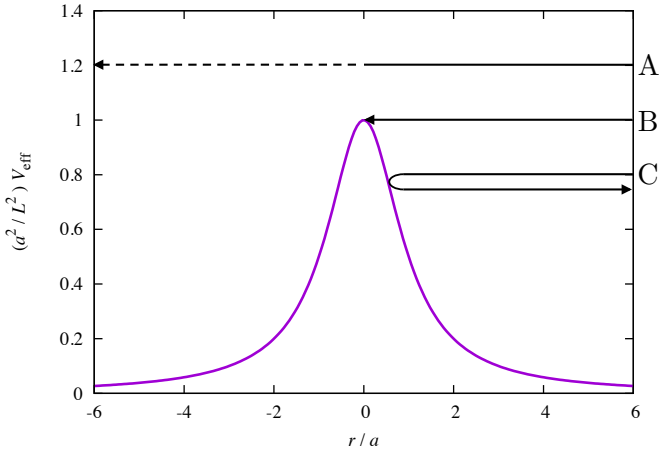

FIG. 2: Effective potential of photons in the Ellis wormhole spacetime. The maximum point at $r = 0$, which indicates the throat of the wormhole, corresponds to the unstable circular orbits. The region for by $r < 0$ is the other side of the spacetime and we use a dashed line for the trajectory in this region.

We show the photon trajectories around the Ellis wormhole in Fig.3. Here we define the rectangle coordinates on the $\theta = \pi/2$ plane as

$$x = r^* \cos\varphi, \quad y = r^* \sin\varphi, \quad r^* = \sqrt{r^2 + a^2} \tag{3.7}$$

These orbits start at the point $r = 300a$ and $\varphi = 0$. The three labels A, B and C correspond to those in Fig.2. Furthermore, the dashed line labeled A represents the photon trajectory in other side.

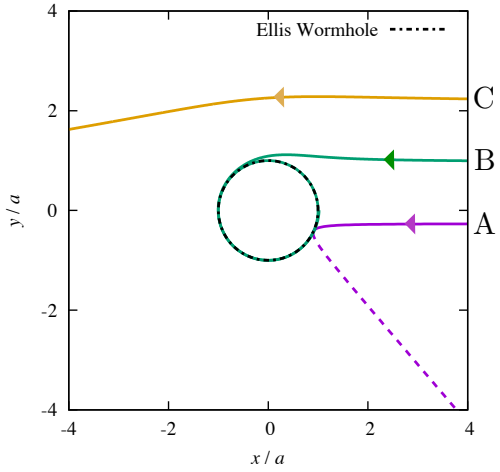

FIG. 3: Photon trajectories around the Ellis wormhole. The coordinates (x, y) are defined as (3.7). The dashed circle denotes the throat of the wormhole. All trajectories end up at the observer at $r = 300a$, $\varphi = 0$. Three labels A, B, and C correspond to those in Fig.2. The dashed line of the label A represents the trajectory on the other side region of the wormhole ($r < 0$).

IV. DYNAMICS OF INTERSTELLAR MEDIUM

In this section, we examine the general relativistic motion of interstellar medium surrounds the Ellis wormhole. Here we assume that the interstellar medium is the perfect fluid and its self-gravity is negligible. The equations of motion of the perfect fluid in Schwarzschild spacetime and their solutions were presented in a textbook by Shapiro and Teukolsky [19]. The dynamics of nonrotating fluid around the Ellis wormhole was discussed in Ref.[17].

A. Thermodynamics

Suppose a local Lorentz frame comoving with fluid particles. Let n, ρ and P be, respectively, the number density, the total energy density, and the pressure of the fluid particles, which are measured in the reference frame. Then the first law of thermodynamics is written as

$$dQ = d\left(\frac{\rho}{n}\right) + Pd\left(\frac{1}{n}\right), \tag{4.1}$$

where dQ is the heat gained per particle. ρ/n and $1/n$ represent, respectively, the energy and the volume per particle. We use the temperature T and the entropy per particle s and $dQ = Tds = 0$ is true on the process of quasistatic (i.e., in thermal equilibrium at all times) and adiabatic. Thus, we obtain

$$0 = d\left(\frac{\rho}{n}\right) + Pd\left(\frac{1}{n}\right), \tag{4.2}$$

We rewrite this equation in the following, simpler form:

$$\frac{d\rho}{dn} = \frac{\rho + P}{n}. \tag{4.3}$$

B. Fluid dynamics

Under the assumption that the particle number is conserved, we obtain the general relativistic continuity equation,

$$(nu^\mu)_{;\mu} = 0, \tag{4.4}$$

where u^μ is the four-velocity of the particle fluid and the semicolon denotes a covariant derivative: $A^\alpha_{;\beta} = \partial_\beta A^\alpha + \Gamma^\alpha_{\beta\gamma} A^\gamma$. Moreover, the energy-momentum tensor is written as

$$T^{\mu\nu} = (\rho + P)u^\mu u^\nu + Pg^{\mu\nu}, \tag{4.5}$$

because we assume that the particle fluid is a perfect fluid. Applying the energy-momentum conservation,

$$T^\nu_{\mu;\nu} = 0, \tag{4.6}$$

to Eq.(4.3) with Eq.(4.5), we obtain the general relativistic Euler equation,

$$(\rho + P)u_{\mu;\nu}u^{\nu} = -P_{,\mu} - u_{\mu}P_{,\nu}u^{\nu}. \tag{4.7}$$

We have two basic equations (4.4) and (4.7), for the general perfect fluid.

C. Slowly rotating dust solutions

The spherically symmetrical and steady-state solutions were derived in Ref.[17]. In this paper we extend our analysis to nonspherical (axially symmetric) cases. We suppose that the four-velocity and number density takes the forms of

$$u^{\mu} = \left(u^t(r,\,\theta),\, u^r(r,\,\theta),\, u^{\theta}(r,\,\theta),\, u^{\varphi}(r,\,\theta)\right), \tag{4.8}$$
$$n = n(r,\,\theta), \tag{4.9}$$

We assume that the interstellar medium is only dust,

$$\rho = mn \quad \text{and} \quad P = 0, \tag{4.10}$$

where m is the mass of the fluid particle. Then, we can rewrite Eq.(4.4) and (4.7) as

$$\frac{\partial}{\partial r}\left[nu^r(r^2+a^2)\sin\theta\right] + \frac{\partial}{\partial\theta}\left[nu^{\theta}(r^2+a^2)\sin\theta\right] = 0, \tag{4.11}$$

$$\frac{\partial u^t}{\partial r}u^r + \frac{\partial u^t}{\partial\theta}u^{\theta} = 0, \tag{4.12}$$

$$\frac{\partial u^r}{\partial r}u^r + \frac{\partial u^r}{\partial\theta}u^{\theta} - r(u^{\theta})^2 - r\sin^2\theta(u^{\varphi})^2 = 0, \tag{4.13}$$

$$(r^2+a^2)\frac{\partial u^{\theta}}{\partial r}u^r + (r^2+a^2)\frac{\partial u^{\theta}}{\partial\theta}u^{\theta} + 2ru^{\theta}u^r - (r^2+a^2)\sin\theta\cos\theta(u^{\varphi})^2 = 0, \tag{4.14}$$

$$(r^2+a^2)\sin^2\theta\frac{\partial u^{\varphi}}{\partial r}u^r + (r^2+a^2)\sin^2\theta\frac{\partial u^{\varphi}}{\partial\theta}u^{\theta} + 2r\sin^2\theta u^{\varphi}u^r + 2(r^2+a^2)\sin\theta\cos\theta u^{\varphi}u^{\theta} = 0. \tag{4.15}$$

Here we assume that dust rotates so slowly that the solution of u^{μ} and n are given by perturbations about the spherically symmetric solution obtained in Ref.[17] as follows.

$$u^t = u^t_0 + u^t_1(r,\,\theta), \tag{4.16}$$
$$u^r = u^r_0 + u^r_1(r,\,\theta), \tag{4.17}$$
$$u^{\theta} = u^{\theta}_1(r,\,\theta), \tag{4.18}$$
$$u^{\varphi} = u^{\varphi}_1(r,\,\theta), \tag{4.19}$$
$$n = n_a\frac{a^2}{r^2+a^2} + n_1(r,\,\theta), \tag{4.20}$$

where u^t_0, u^r_0 and n_a are constants of the unperturbed (i.e., spherically symmetric) solutions, and u^t_1, u^r_1, u^{θ}_1, u^{φ}_1 and n are perturbed quantities caused by dust rotation.

We substitute these expressions into Eqs.(4.11) - (4.15) and solve them up to the first order of the perturbed quantities. Then we obtain the solution of u^t_1, u^r_1, u^{θ}_1, u^{φ}_1 and n_1 as

$$u^t_1 = \frac{u^r_0}{u^t_0}f^r(\theta), \tag{4.21}$$
$$u^r_1 = f^r(\theta), \tag{4.22}$$
$$u^{\theta}_1 = \frac{a^2}{r^2+a^2}f^{\theta}(\theta), \tag{4.23}$$
$$u^{\varphi}_1 = \frac{a^2}{r^2+a^2}f^{\varphi}(\theta), \tag{4.24}$$
$$n_1 = \frac{n_a}{u^r_0}\frac{a^2}{r^2+a^2}\left\{a\cdot\tan^{-1}\left(\frac{r}{a}\right) + C(\theta)\right\}N(\theta), \tag{4.25}$$

where f^r, f^{θ}, f^{φ} and C are arbitrary functions of θ, and N is defined as

$$N(\theta) \equiv -\frac{1}{\sin\theta}\frac{\partial}{\partial\theta}\left[f^{\theta}\sin\theta\right]. \tag{4.26}$$

From the regularity condition on the poles ($\theta = 0, \pi$), $N(\theta)$ must satisfy

$$\left.\frac{dN}{d\theta}\right|_{\theta=0} = \left.\frac{dN}{d\theta}\right|_{\theta=\phi} = 0. \tag{4.27}$$

As a solution of $f(\theta)$ which satisfies (4.27), we adopt

$$f^{\theta}(\theta) = f^{\theta}_0\sin(k\theta), \quad \{k \in \mathbb{Z}^+\}, \tag{4.28}$$

where f^{θ}_0 is a dimensionless constant. Then, we can rewrite Eq.(4.26) as

$$N(\theta) = -f^{\theta}_0\left[k\cos(k\theta) + \sin(k\theta)\cot\theta\right]. \tag{4.29}$$

Here we suppose that dust is distributed reflection-symmetrically with respect to the $\theta = \pi/2$ plane, that is, k is even.

Figure 4 is the contour map of the dust density $n(r,\,\theta)/n_a$. The rectangle coordinates $(x,\,z)$ are defined as

$$x = \sqrt{r^2+a^2}\sin\theta, \quad z = \sqrt{r^2+a^2}\cos\theta. \tag{4.30}$$

This means that the wormhole throat corresponds to the circle $x^2 + z^2 = a^2$. No real spacetime exists in the black region of $x^2 + z^2 < a^2$. We set $u^r_0 = -0.1$ and $C(\theta) = 0$, and illustrate four cases, $(f^{\theta}_0,\, k) = (-0.02,\, 2)$, $(0.02,\, 2)$, $(-0.02,\, 4)$ and $(0.02,\, 4)$. We find the following characteristics, which are caused by the effect of rotation.

- While the density peak is located at the throat ($r = a$) in the case of spherically symmetry, it deviates slightly to the outer side of the throat in the present case.
- The high density region is not spherical but distorted; the shape varies depending on the values of $(f^{\theta}_0,\, k)$.

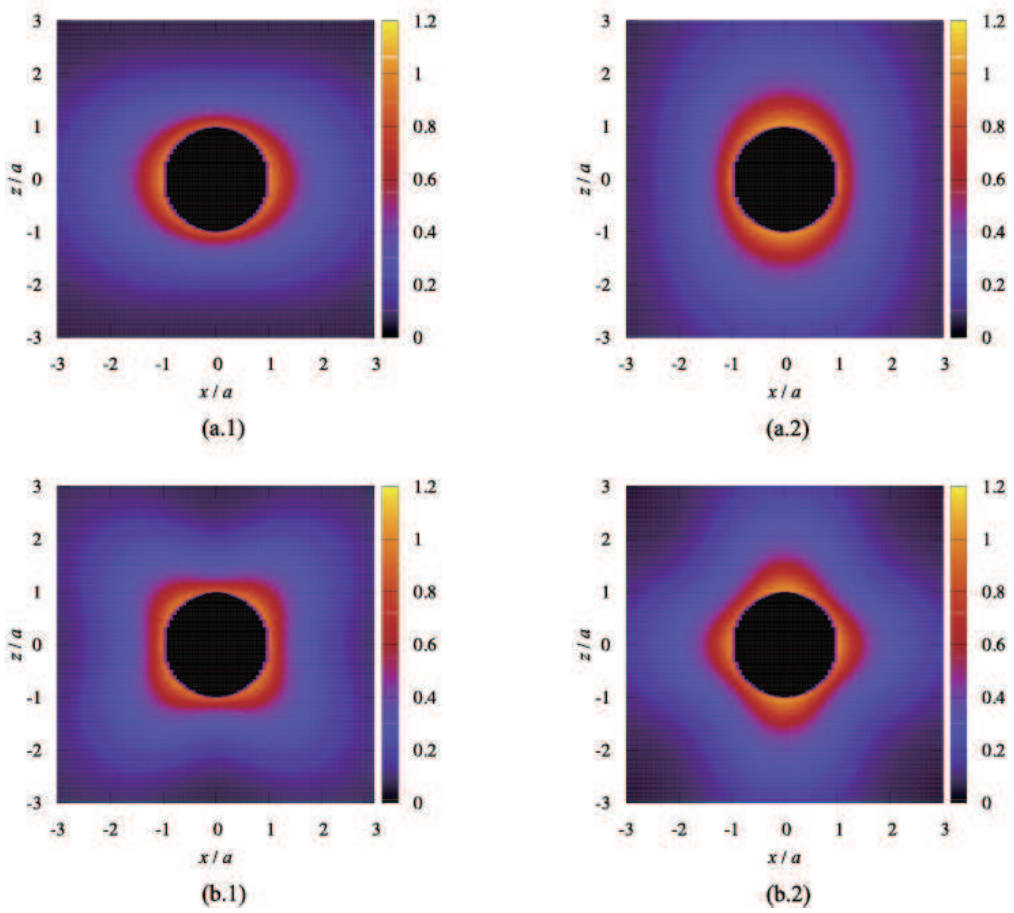

FIG. 4: Contour map of the dust density $n(r, \theta)/n_a$. The rectangle coordinates (x, z) are defined as (4.30) and hence the wormhole throat corresponds to the circle $x^2 + z^2 = a^2$. No real spacetime exists in the black region of $x^2 + z^2 < a^2$. We set $u_0^r = -0.1$ and $C(\theta) = 0$, and illustrate four cases, $(f_0^\theta, k) = (-0.02, 2)$, $(0.02, 2)$, $(-0.02, 4)$ and $(0.02, 4)$, in (a.1), (a.2), (b.1), and (b2), respectively.

V. WORMHOLE SHADOWS

We investigate the optical images of dust surrounding the wormhole, using the axially symmetric solutions obtained in Sec. IV.

A. Apparent position of optical sources

Gravity refracts light rays in general relativity. This phenomenon is known as gravitational lensing. We may see a light source as if it was another position. To obtain optical images, we have to not only solve the null geodesic equations, but also give the relation between the null vector at the observer and the apparent potion of the source.

We put an Ellis wormhole at the origin, an observer at $\vec{r}_{\rm obs}$, as shown in Fig. 5. Plane A is defined as the plane which is normal to $\vec{r}_{\rm obs}$ and contains the origin. We denote the intersection of Plane A with the tangent to the ray at the observer by $\vec{\alpha}$, which corresponds the apparent position of a light source, as shown in (a). Figure 5 (b) is the same diagram as (a) but the standpoint is on the y-axis. We accord the rotational axis of dust to z-axis and denote the angle between it and $\vec{r}_{\rm obs}$ as i. We put the observer on the x-z plane.

Then the two vectors $\vec{r}_{\rm obs}$ and $\vec{\alpha}$ are expressed as

$$\vec{r}_{\rm obs} = (r_{\rm obs}\sin i,\ 0,\ r_{\rm obs}\cos i), \tag{5.1}$$
$$\vec{\alpha} = (-\alpha_z\cos i,\ \alpha_y,\ \alpha_z\sin i), \tag{5.2}$$

where $r_{\rm obs} \equiv |\vec{r}_{\rm obs}|$. Thus, the equations of the line which connects the two points are written as

$$\frac{x - r_{\rm obs}\sin i}{r_{\rm obs}\sin i + \alpha_z\cos i} = -\frac{y}{\alpha_y} = \frac{z - r_{\rm obs}\cos i}{r_{\rm obs}\cos i - \alpha_z\sin i}. \tag{5.3}$$

Differentiating the equations and taking the limit ($r \to$

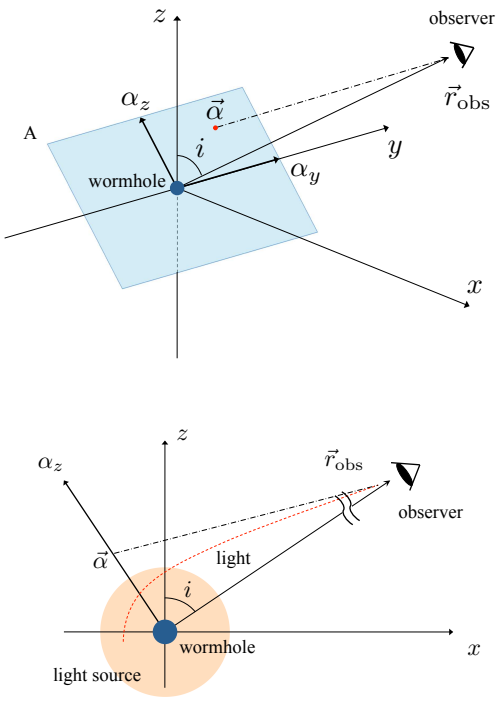

(b)

FIG. 5: Positional relationship among the wormhole, the apparent position of a light source, and the observer. (a) Plane A is defined as the plane which is normal to $\vec{r}_{\rm obs}$ and contains the origin. We denote the intersection of Plane A with the tangent to the ray at the observer by $\vec{\alpha}$, which corresponds the apparent position of a light source. (b) is the same diagram as (a) but the standpoint is on the y-axis. We accord the rotational axis of dust to z-axis and denote the angle between it and $\vec{r}_{\rm obs}$ as i. We put the observer on the x-z plane.

$\vec{r}_{\rm obs}$, $\theta \to i$, $\varphi \to 0$), we obtain

$$\left(\sin i + r_{\rm obs}\cos i\,\frac{d\theta}{dr}\right)\alpha_y(r_{\rm obs}\cos i - \alpha_z \sin i)$$
$$= -r_{\rm obs}\sin i\,\frac{d\varphi}{dr}(r_{\rm obs}\sin i + \alpha_z\cos i)(r_{\rm obs}\sin i + \alpha_z \sin i)$$
$$= \left(\cos i - r_{\rm obs}\sin i\,\frac{d\theta}{dr}\right)\alpha_y(r_{\rm obs}\sin i + \alpha_z\cos i). \quad (5.4)$$

We solve these equations for α_y and α_z:

$$\alpha_y = -{r_{\rm obs}}^2\sin i\,\frac{d\varphi}{dr} = -{r_{\rm obs}}^2\sin i\,\frac{k^\varphi(\vec{r}_{\rm obs})}{k^r(\vec{r}_{\rm obs})}, \quad (5.5)$$

$$\alpha_z = {r_{\rm obs}}^2\frac{d\theta}{dr} = {r_{\rm obs}}^2\frac{k^\theta(\vec{r}_{\rm obs})}{k^r(\vec{r}_{\rm obs})}. \quad (5.6)$$

We thus obtain the relation between the apparent position of a light source and the null vector at the observer.

B. Radiation intensity

To calculate the observed intensity of radiation emitted from optically thin gas, we solve the general relativistic radiative transfer equation, which is generally expressed as [18],

$$\frac{d\mathfrak{J}}{d\lambda} = \frac{\eta(\nu)}{\nu^2} - \nu\chi(\nu)\mathfrak{J}, \qquad \mathfrak{J} \equiv \frac{I(\nu)}{\nu^3} \quad (5.7)$$

where ν is the photon frequency, $I(\nu)$ is the specific intensity, $\mathfrak{J}$ is the invariant intensity, $\eta(\nu)$ is the emission coefficient and $\chi(\nu)$ is the absorption coefficient. Because Eq.(5.7) is the differential equation along null geodesics, we should solve the null geodesic equations simultaneously.

Here we make the following assumptions, for simplicity:

- The dust does not absorb radiation, i.e., $\chi(\nu) = 0$.
- $\eta(\nu)$ is proportional to the dust density which is measured along the null geodesics, i.e., $\eta(\nu)d\lambda \propto \rho u_\mu dx^\mu$.

Introducing a positive factor $H(\nu)$, which is proportional to the spectrum of the dust sources, we express $\eta(\nu)$ as

$$\eta(\nu)d\lambda = -H(\nu)\rho u_\mu dx^\mu. \quad (5.8)$$

With these assumptions we can integrate (5.7) as

$$\mathfrak{J} = -\int \frac{H(\nu)}{\nu^2}\rho u_\mu dx^\mu. \quad (5.9)$$

The integration in Eq.(5.9) should be performed alongside the null geodesics. The frequency measured by observers comoving with dust particles is given by

$$\nu = -u_\mu k^\mu. \quad (5.10)$$

Generally we should fix the spectrum of the dust sources, i.e., $H(\nu)$. Here, for simplicity, we assume a flat spectrum, $H(\nu) = \text{const}$.

C. Numerical analysis

We compute the intensity distribution as follows:

(i). Put the observer at $r_{\rm obs} = 300a$ and $i = \pi/2$.

(ii). For given $\vec{\alpha}$, we solve Eqs.(5.5) and (5.6) to obtain $k^\varphi(\vec{r}_{\rm obs})$ and $k^\theta(\vec{r}_{\rm obs})$ with fixing $k^r(\vec{r}_{\rm obs}) = 1.0$. Then we solve the null geodesic equations from the observer and obtain the frequencies ν at each points by Eq.(5.10). We can choose a value of the initial (observed) frequency $\nu_{\rm obs}$ arbitrarily because the ratio of $\nu_{\rm obs}$ to the emitted frequency $\nu_{\rm emit}$ does not depend on $\nu_{\rm obs}$.

(iii). With the values of ν at each point, which is determined by the null geodesic equations, we integrate Eq.(5.9) to obtain the intensity I. We adopt the fourth-order Runge-Kutta method for all integrations.

(iv). We continue the integrations until $r_{\rm obs} = 300a$ again, where the gas density is sufficiently small.

(v). Iterate (ii) $\sim$ (iv) by changing the value of $\vec{\alpha}$.

We adopt the dust solutions (4.21) - (4.25) with the parameters, $u_0^r = -0.1$, $f^r = 0$, $f^\varphi = 0.02$ and $C(\theta) = 0$. We calculate for four cases, $(f_0^\theta,\, k) = (-0.02,\, 2)$, $(0.02,\, 2)$, $(-0.02,\, 4)$ and $(0.02,\, 4)$.

We show the results of our numerical calculations in Fig. 6. We find the following phenomena.

- A bright ring appears on each case.
- The bright ring looks distorted due to rotation.
- There appear weakly luminous complex patterns, which vary depending on the values of $(f_0^\theta,\, k)$.

The first phenomenon is due to the existence of unstable circular orbits of photons. The second phenomenon occurs because the equatorial region is more dense, as discussed in Sec. IV.C. The third phenomenon is due to the existence of the other side region of the wormhole.

Figure 7 shows the different case from the above computations. Here, we compute on the case of $i = \pi/4$, and other parameters are same as Figs. 6(a.1) and (b.1): (1) is $(f_0^\theta,\, k) = (-0.02,\, 2)$ and (2) is $(f_0^\theta,\, k) = (-0.02,\, 4)$. The patterns are more complex than it on the case of Fig.6.

VI. CONCLUDING REMARKS

This work is an extension of our previous work which studied wormhole shadows in nonrotating dust. In the case of spherically symmetric dust, we had found two types of solutions: $u^r = 0$ and $\rho =$ arbitrary function of r (Type I) and $u^r \neq 0$, $\rho \propto (r^2 + a^2)^{-1}$ (Type II). First, we derived steady-state solutions of rotating dust and more general medium surrounding the wormhole by solving general relativistic Euler equations. We consider the perturbation from the type II of nonrotating solution. Our solutions for rotating dust density (4.20) with (4.25) has a peak at a little outside of the throat ($r > a$). This is the clearly different point from the nonrotating dust.

Next, solving radiation transfer equations along null geodesics, we investigated the optical images of the wormhole surrounded by dust for the above steady-state rotating solutions. A bright ring appears in the image, just as in Schwarzschild spacetime, because the wormhole spacetime possesses unstable circular orbits of photons. The bright ring looks distorted because the equatorial region is more dense. Additionally, there appears a weakly luminous pattern differently depnding on on the parameters of $(f_0^\theta,\, k)$. This pattern is due to the existence of the other side region of the wormhole.

Because our method is general, it is applicable to other astronomical bodies (e.g. gravastars [20]) for researches of these optical images. Shodows of wormholes and other compact objects could be detected with high-resolution VLBI observations in the near future.

Acknowledgments

We thank F. Abe, K. Fujisawa, T. Harada, H. Saida and K. Shiraishi for useful discussions.

[1] A. Einstein and N. Rosen, Phys. Rev. **48**, 73 (1935).
[2] H. G. Elis, J. Math. Phys. (N.Y.) **14**, 104 (1973).
[3] M. S. Morris and K. S. Thorne, Am. J. Phys. **56**, 395 (1988).
[4] H. Shinkai and S. A. Hayward, Phys. Rev. D **66**, 044005 (2002).
[5] J. A. González, F. S. Guzmán, and O. Sarbach, Classical Quantum Gravity **26**, 015010 (2009); *ibid.*, 015011 (2009).
[6] A. Das and S. Kar, Classical Quantum Gravity **22**, 3045 (2005).
[7] L. Chetouani and G. Clement, Gen. Relativ. Gravit. **16**, 111 (1984); G. Clement, Int. J. Theor. Phys. **23**, 335 (1984); V. Perlick, Phys. Rev. D **69**, 064017 (2004); K. K. Nandi, Y.-Z. Zhang, and A. V. Zakharov, Phys. Rev. D **74**, 024020 (2006); T. K. Dey and S. Sen, Mod. Phys. Lett. A **23**, 953 (2008); K. Nakajima and H. Asada, Phys.Rev. D **85**, 107501 (2012); N. Tsukamoto and T. Harada, Phys. Rev. D **87**, 024024 (2013).
[8] J. G. Cramer, R. L. Forward, M. S. Morris *et al.*, Phys. Rev. D **51**, 3117 (1995).
[9] D. F. Torres, G. E. Romero, and L. A. Anchordoqui, Phys. Rev. D **58**, 123001 (1998); M. Safonova, D. F. Torres, and G. E. Romero, Phys. Rev. D **65**, 023001 (2001); M. B. Bogdanov and A. M. Cherepashchuk, Astrophys. Space Sci. **317**, 181 (2008); F. Abe, Astrophys. J. **725**, 787 (2010); T. Kitamura, K. Nakajima, and H. Asada, Phys. Rev. D **87**, 027501 (2013).
[10] Y. Toki, T. Kitamura, H. Asada, and F. Abe, Astrophys. J. **740**, 121 (2011); N. Tsukamoto, T. Harada, and K. Yajima, Phys. Rev. D **86**, 104062 (2012).
[11] C.-M. Yoo, T. Harada, and N. Tsukamoto, Phys. Rev. D

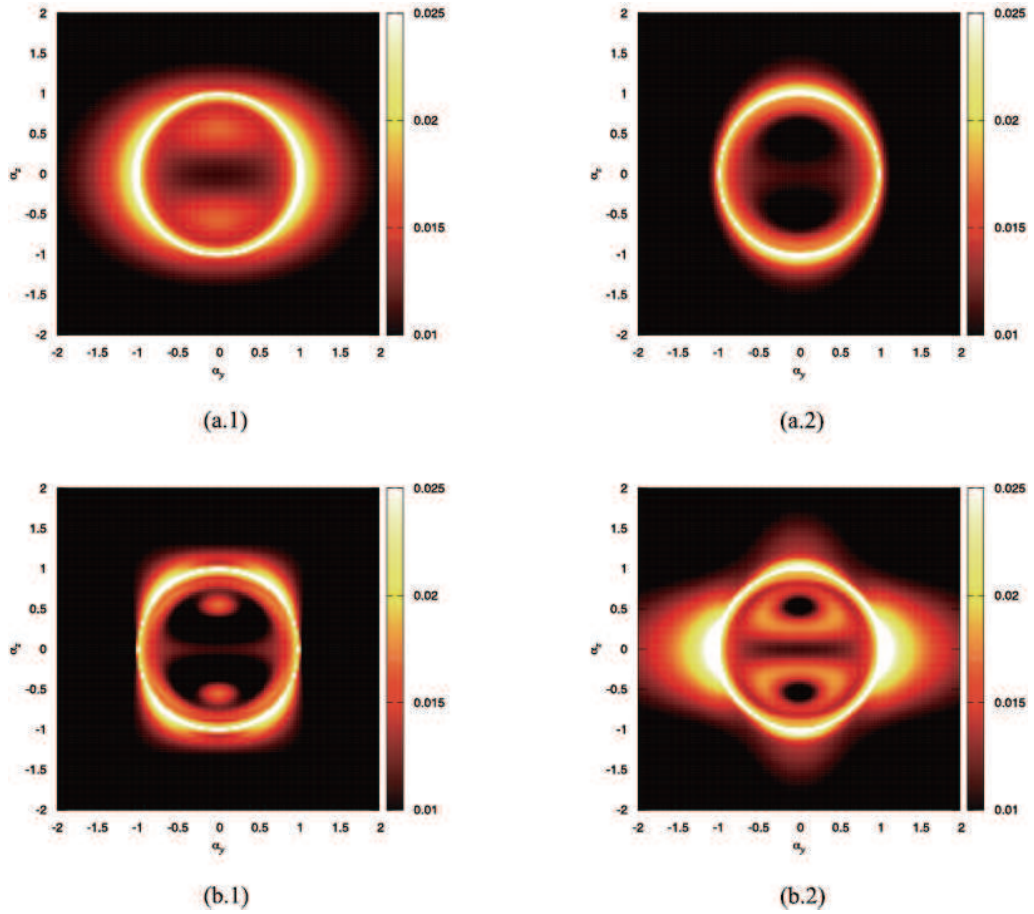

FIG. 6: Optical images of the wormhole surrounded by rotating dust for several cases of $(f_0^\theta,\, k)$: (a.1), (a.2), (b.1) and (b.2) show the cases of $(-0.02,\, 2)$, $(0.02,\, 2)$, $(-0.02,\, 4)$ and $(0.02,\, 4)$, respectively. A bright ring looks distorted like the high density region of dust. Additionally, there appears a weakly luminous pattern differently depending on the value of $(f_0^\theta,\, k)$.

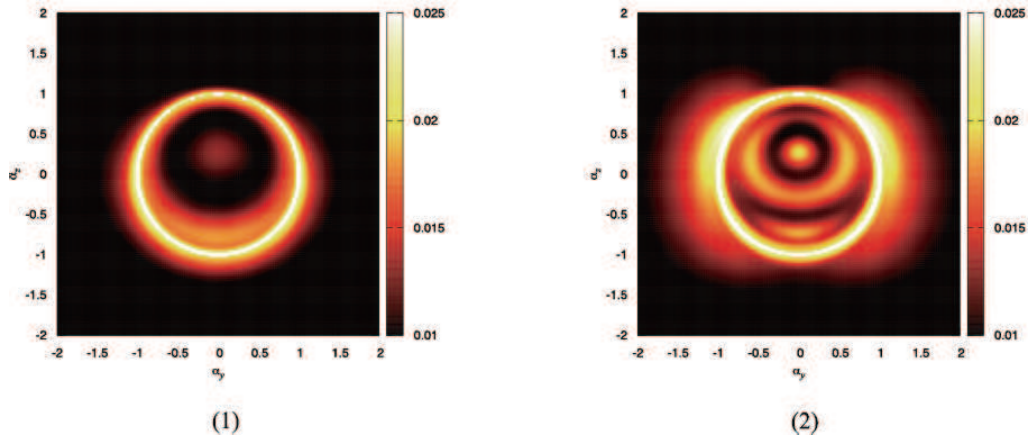

FIG. 7: Optical images on the case of $i = \pi/4$: (1) is $(f_0^\theta,\, k) = (-0.02,\, 2)$, (2) is $(f_0^\theta,\, k) = (-0.02,\, 4)$. Other parameters are same values as the case of Fig.6. The patterns are more complex than it on the case of Fig.6.

87, 084045 (2013).

[12] J. M. Bardeen, IN *Les Astres Occlus*, edited by C. DeWitt and B. S. DeWitt, (Gordon and Breach, New York, 1973), p. 215.

[13] R. Takahashi, Astrophys. J. **611**, 996 (2004); Pub. Astron. Soc. Jpn. **57**, 273 (2005).

[14] M. Miyoshi, J.K. Ishitsuka, S. Kameno, Z. Shen, and S. Horiuchi, Prog. Theor. Phys. Suppl. **155**, 186 (2004); H. Hirabayashi *et al.*, arXiv:astro-ph/0501020; S. Doeleman *et al.*, Nature (London) **455**, 78 (2008); M. Miyoshi *et*

al., Pub. National Astronomical Observatory Japan **10**, 15 (2007); Astron. Soc. Pac. Conf. Ser., **439** 279 (2011); H. Falcke, F. Melia and Eric Agol, Astrophys. J. **528**, L13 (2000).

[15] P. G. Nedkova, V. Tinchev, and S. S. Yazadjiev, Phys. Rev. D **88**, 124019 (2013).

[16] O. Sarbach and T. Zannias, AIP Conf. Proc. **1473**, 223 (2012); P. Taylor, Phys. Rev. D **90**, 024057 (2014).

[17] T. Ohgami and N. Sakai, Phys. Rev. D **91**, 124020 (2015).

[18] D. Mihalas and B. W. Mihalas, *Foundations of Radiation Hydrodynamics* (Dover Pub., New York, 1999).

[19] S. L. Shapiro and S. A. Teukolsky, *Black Holes, White Dwarfs and Neutron Stars: The Physics of Compact Objects* (John Wiley & Sons, New York, 1983).

[20] N. Sakai, H. Saida, and T. Tamaki, Phys. Rev. D 90, 104013 (2014).